

Current reversals and metastable states in the infinite Bose-Hubbard chain with local particle loss

M. Kiefer-Emmanouilidis^{1,2} and J. Sirker¹

¹University of Manitoba, Department of Physics, Winnipeg

²Technische Universität Kaiserslautern, Department of Physics, Kaiserslautern

(Dated: October 10, 2018)

We present an algorithm which combines the quantum trajectory approach to open quantum systems with a density-matrix renormalization group scheme for infinite one-dimensional lattice systems. We apply this method to investigate the long-time dynamics in the Bose-Hubbard model with local particle loss starting from a Mott-insulating initial state with one boson per site. While the short-time dynamics can be described even quantitatively by an equation of motion (EOM) approach at the mean-field level, many-body interactions lead to unexpected effects at intermediate and long times: local particle currents far away from the dissipative site start to reverse direction ultimately leading to a metastable state with a total particle current pointing away from the lossy site. An alternative EOM approach based on an effective fermion model shows that the reversal of currents can be understood qualitatively by the creation of holon-doublon pairs at the edge of the region of reduced particle density. The doublons are then able to escape while the holes move towards the dissipative site, a process reminiscent—in a loose sense—of Hawking radiation.

PACS numbers:

I. INTRODUCTION

No quantum system is perfectly isolated. Coherent dynamics as described by Schrödinger's equation lasts only over a finite timescale before dissipation leads to decoherence. While dissipation is an intrinsic process in solid state systems determined by the properties of the material, the advent of quantum gases in optical lattices¹ has made it possible to study lattice systems where dissipation can be controlled to a certain degree and used as a tool to manipulate the quantum state.²⁻⁴

Experimentally it has been shown, for example, that strong dissipation in the form of two-body losses can model a Pauli exclusion principle, fermionizing a system.⁵ Using an electron beam, a controlled local particle loss process has been realized for a Bose-Einstein condensate (BEC) providing direct evidence for the quantum Zeno effect.⁶ Furthermore, local particle loss has been used to create a tunnel junction between two Bose-Einstein condensates (BEC) and negative differential conductance has been observed.⁷ For a one-dimensional array of BEC's with a single lossy site it has also been shown that a transition from a superfluid to a resistive state can be driven by tuning the loss rate γ with a bistability occurring at intermediate γ .⁸

Theoretically, local particle loss in the non-interacting Bose-Hubbard model has been studied in Ref.9 while the interacting case has been investigated numerically using time-dependent density-matrix renormalization group (tDMRG) algorithms.¹⁰ The quantum Zeno dynamics which has been observed in these simulations for local particle loss rates γ much larger than the hopping amplitude J can be understood in a perturbative approach based on adiabatic elimination.¹¹ Global three-body loss processes have also been simulated by tDMRG algorithms and have been shown to give rise to effective

three-body hard-core interactions.¹² Quite recently, also the cases of interacting spinless fermions with disorder and local particle loss¹³ and of the Bose-Hubbard model with dephasing have been studied.¹⁴

In this paper we will consider open quantum systems which can be described in Markov approximation leading to the following general Lindblad master equation (LME) for the density matrix $\hat{\rho}$

$$\frac{d}{dt}\hat{\rho} = -i[\hat{H}, \hat{\rho}] + \sum_{j=1}^L \gamma_j \left(\hat{A}_j \hat{\rho} \hat{A}_j^\dagger - \frac{1}{2} \{ \hat{A}_j^\dagger \hat{A}_j, \hat{\rho} \} \right). \quad (1)$$

Here H is the Hamiltonian, \hat{A}_j the operator describing local dissipation at site j of a lattice of length L with rate γ_j , and $\{.,.\}$ the anti-commutator.

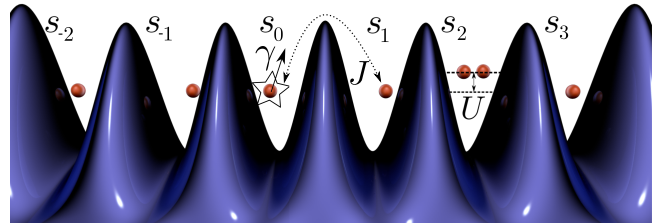


FIG. 1: A one-dimensional lattice model with hopping amplitude J and onsite interaction U . At site $j = 0$ particles escape the lattice with loss rate γ .

Part of the progress in studying the dynamics of one-dimensional open many-body systems is currently driven by numerical renormalisation group algorithms such as tDMRG¹⁵⁻¹⁷ and the time-evolving block decimation (TEBD)¹⁸⁻²⁰ for finite lattice systems. For local particle loss neither method unfortunately leads to non-equilibrium steady states (NESS) other than the vacuum because the number of particles is also typically finite.

The same problem also exists for metastable states established at long time scales.²¹ Here we present a numerical scheme combining the quantum trajectory (QT) approach^{3,22–24} with the Light Cone Renormalization Group (LCRG)²⁵ to treat open one-dimensional quantum systems directly in the thermodynamic limit. This will allow, in particular, to study the dynamics in the Bose-Hubbard model with local particle loss shown in Fig. 1 at times $t \gg J/\gamma$.

Our paper is organized as follows. In Sec. II we introduce the Bose-Hubbard chain with local particle loss. We then discuss equation of motion (EOM) approaches in Sec. II A before describing the numerical renormalization group algorithm to simulate the Lindblad dynamics for infinite system size in Sec. II B. The results of both methods are presented in Sec. III which includes a discussion of the density and current profiles, the particle loss rate, and the evolution of the density-density correlations. Sec. IV is devoted to a short summary and conclusions.

II. MODEL AND METHODS

In the following, we will consider the Bose-Hubbard Hamiltonian

$$H = -J \sum_j \left(\hat{b}_j^\dagger \hat{b}_{j+1} + h.c. \right) + \frac{U}{2} \sum_j \hat{n}_j (\hat{n}_j - 1) - \mu \sum_j \hat{n}_j, \quad (2)$$

where $\hat{b}_j^{(\dagger)}$ is the bosonic annihilation (creation) operator acting at site j , and $\hat{n}_j = \hat{b}_j^\dagger \hat{b}_j$ is the number operator. The bosonic operators fulfill the commutation relations $[\hat{b}_i, \hat{b}_j^\dagger] = \delta_{ij}$ and $[\hat{b}_i^\dagger, \hat{b}_j^\dagger] = [\hat{b}_i, \hat{b}_j] = 0$, where δ_{ij} is the Kronecker delta. J is the hopping amplitude and U the onsite Hubbard interaction which is assumed to be positive corresponding to repulsive interactions between atoms on the same site. μ is the chemical potential. We assume that the system at time $t = 0$ is prepared in the ground state of the closed system and concentrate, in particular, on initial states with commensurate filling $\langle n_j \rangle = 1$ deep in the Mott insulating phase ($U \gg 3J$). The non-unitary dynamics is then described by the LME

$$\frac{d}{dt} \hat{\rho} = -i[\hat{H}_{\text{BH}}, \hat{\rho}] + \gamma \left(\hat{b}_0 \hat{\rho} \hat{b}_0^\dagger - \frac{1}{2} \left\{ \hat{b}_0 \hat{b}_0, \hat{\rho} \right\} \right), \quad (3)$$

which is a special case of the general LME, Eq. (1), with dissipation—in terms of a local particle loss process—limited to site $j = 0$. The model is motivated by recent experiments on cold atomic gases where an electron beam has been used to ionize and eject particles from the gas with single site resolution.^{7,8,26}

A. Equation of motion

The time-dependence of an observable $\hat{X}(t)$ in an open quantum system modeled by an LME is given by the

EOM

$$\frac{d}{dt} \hat{X} = i[\hat{H}, \hat{X}] + \sum_{j=1}^L \gamma_j \left(\hat{A}_j^\dagger \hat{X} \hat{A}_j - \frac{1}{2} \left\{ \hat{A}_i^\dagger \hat{A}_i, \hat{X} \right\} \right). \quad (4)$$

For particle loss $\hat{A}_j = \hat{b}_j$ and without the Hubbard interaction U the EOM closes and the dynamics can be obtained exactly by numerically integrating the EOM. For finite interactions, on the other hand, terms will in general be generated on the right hand side of Eq. (4) which contain more bosonic operators than the observable \hat{X} leading to an infinite hierarchy of equations. This hierarchy has to be truncated in practice by using a mean-field decoupling of higher order correlators. Nevertheless, for short times such an approach often yields a good approximation of the non-equilibrium dynamics of local observables.

1. Direct decoupling

We are interested, in particular, in the time evolution of the density profiles $\langle n_j \rangle(t)$ and current profiles $\langle \mathcal{J}_j \rangle(t)$. Evaluating Eq. (4) for the two-point function $\sigma_{jk}(t) = \langle \hat{b}_j^\dagger \hat{b}_k \rangle(t)$ leads to^{27,28}

$$\begin{aligned} i \frac{d}{dt} \sigma_{jk} &= -J (\sigma_{j,k+1} + \sigma_{j,k-1} - \sigma_{j+1,k} - \sigma_{j-1,k}) \\ &+ U \left(\langle a_j^\dagger a_k^\dagger a_k a_k \rangle - \langle a_j^\dagger a_j^\dagger a_j a_k \rangle \right) \\ &- i \frac{\gamma_0}{2} (\delta_{j,0} + \delta_{k,0}) \sigma_{jk}. \end{aligned} \quad (5)$$

In a first order approximation, we can simply use a Hartree-Fock decoupling of the quartic terms

$$\langle a_j^\dagger a_k^\dagger a_k a_k \rangle - \langle a_j^\dagger a_j^\dagger a_j a_k \rangle \rightarrow \sigma_{kk} \sigma_{jk} - \sigma_{jj} \sigma_{jk}. \quad (6)$$

Within this decoupling scheme, Eq. (5) can now be solved numerically. To improve on this approximation and to check how sensitive the solution is to the decoupling, we also consider the EOM for a general four-point correlator $\theta_{ijkl} = \langle \hat{b}_i^\dagger \hat{b}_j^\dagger \hat{b}_k \hat{b}_l \rangle$:

$$\begin{aligned} i \frac{d}{dt} \theta_{ijkl} &= -J (\theta_{i,j,k-1,l} + \theta_{i,j,k+1,l} + \theta_{i,j,k,l-1} \\ &+ \theta_{i,j,k,l+1} - \theta_{i-1,j,k,l} - \theta_{i+1,j,k,l} - \theta_{i,j-1,k,l} - \theta_{i,j+1,k,l}) \\ &+ U \left(\langle \hat{b}_i^\dagger \hat{b}_j^\dagger \hat{b}_j^\dagger \hat{b}_j \hat{b}_k \hat{b}_l \rangle + \langle \hat{b}_i^\dagger \hat{b}_i^\dagger \hat{b}_i \hat{b}_j^\dagger \hat{b}_k \hat{b}_l \rangle \right. \\ &- \left. \langle \hat{b}_i^\dagger \hat{b}_j^\dagger \hat{b}_k \hat{b}_l^\dagger \hat{b}_l \hat{b}_l \rangle - \langle \hat{b}_i^\dagger \hat{b}_j^\dagger \hat{b}_k^\dagger \hat{b}_l \hat{b}_k \hat{b}_k \rangle \right) \\ &- i \frac{\gamma_0}{2} (\delta_{i,0} + \delta_{j,0} + \delta_{k,0} + \delta_{l,0}) \theta_{ijkl}. \end{aligned} \quad (7)$$

To close the system of EOM's, Eqs. (5,7), we now decouple the six-point correlators into 4-point and two-point correlators

$$\begin{aligned}
& U \left(\langle b_i^\dagger b_j^\dagger b_j^\dagger b_k b_l \rangle + \langle b_i^\dagger b_i^\dagger b_j^\dagger b_k b_l \rangle \right. \\
& \left. - \langle b_i^\dagger b_j^\dagger b_k b_l^\dagger b_l \rangle - \langle b_i^\dagger b_j^\dagger b_k^\dagger b_l b_k b_k \rangle \right) \\
& \rightarrow U \theta_{ijkl} (\sigma_{jj} + \sigma_{ii} - \sigma_{kk} - \sigma_{ll}). \quad (8)
\end{aligned}$$

In the following, we denote the EOM (5) with the Hartree-Fock decoupling (6) as first order approximation and the EOM's (5,7) with the decoupling scheme (8) as second order approximation.

2. Effective fermionic model

Alternatively, an EOM approach can be formulated by first mapping the BHM for strong repulsive interactions onto an effective fermionic model (EFM).^{14,29-31} The main idea is to limit the local Hilbert space to states with $n = 0, 1, 2$ particles. We can then interpret the state $|1\rangle$ as the vacuum, the holon as a fermion with spin down, and the doublon as a fermion with spin up. The fermionic statistics ensures that not more than holon or doublon can occupy the same site. Formally, the mapping is given by

$$b_j^\dagger = Z_j \sqrt{2} c_{j\uparrow}^\dagger (1 - n_{j\downarrow}) + Z_j c_{j\downarrow} (1 - n_{j\uparrow}) \quad (9)$$

with $n_{j\sigma} = c_{j\sigma}^\dagger c_{j\sigma}$ and the Jordan-Wigner string $Z_j = \prod_{j' < j} \exp(i\pi \sum_{\sigma} n_{j'\sigma})$. The local density operator then reads

$$b_j^\dagger b_j = 1 + n_{j\uparrow} - n_{j\downarrow} \quad (10)$$

where the hard-core constraints have to be properly taken into account. In this approximation, the BHM Hamiltonian is given by

$$\begin{aligned}
H &= -J \sum_j \left[2c_{j\uparrow}^\dagger c_{j+1\uparrow} + c_{j\downarrow}^\dagger c_{j+1\downarrow} + h.c. \right] \\
&+ \sqrt{2}J \sum_j \left[c_{j\uparrow}^\dagger c_{j+1\downarrow}^\dagger + c_{j\downarrow}^\dagger c_{j+1\uparrow}^\dagger + h.c. \right] \\
&- \frac{U}{2} \sum_j (n_{j\uparrow} + n_{j\downarrow}) + V \sum_j n_{j\uparrow} n_{j\downarrow} \quad (11)
\end{aligned}$$

with $V \rightarrow \infty$ required to project out unphysical states where a holon and a doublon occupy the same site. In the following we drop this constraint which is a reasonable lowest order approximation if the number of holons and doublons in the system is very small. To derive the EOM's, we can either diagonalize the Hamiltonian first by a Fourier and a Bogoliubov transform or work directly with the Hamiltonian (11) in position space. We choose to do the latter here, in which case we also have to consider the EOM's for the 'pairing terms', see second line of (11). We introduce the following shorthand notation: $h_{kl} = \langle c_{k\downarrow}^\dagger c_{l\downarrow} \rangle$, $d_{kl} = \langle c_{k\uparrow}^\dagger c_{l\uparrow} \rangle$, $a_{kl} = \langle c_{k\downarrow} c_{l\uparrow} \rangle$, and $\bar{a}_{kl} = \langle c_{k\downarrow}^\dagger c_{l\uparrow}^\dagger \rangle = -a_{kl}^\dagger$. For the doublon correlator the EOM then reads

$$\begin{aligned}
i\dot{d}_{kl} &= 2J(d_{k-1l} - d_{kl+1} + d_{k+1l} - d_{kl-1}) \\
&- \sqrt{2}J(a_{k+1l} + \bar{a}_{l+1k} - \bar{a}_{l-1k} - a_{k-1l}) \\
&- i\gamma_0(\delta_{k0} + \delta_{l0})d_{kl}(1 - \langle n_{0\downarrow} \rangle) \quad (12)
\end{aligned}$$

and for the holon

$$\begin{aligned}
i\dot{h}_{kl} &= J(h_{k-1l} - h_{kl+1} + h_{k+1l} - h_{kl-1}) \\
&- \sqrt{2}J(-a_{lk+1} - \bar{a}_{kl+1} + \bar{a}_{kl-1} + a_{lk-1}) \\
&+ i\gamma_0[\delta_{k0}\delta_{l0} - \frac{1}{2}(\delta_{k0} + \delta_{l0})h_{kl}](1 - \langle n_{0\uparrow} \rangle) \\
&- i\gamma_0\sqrt{2}\delta_{l0}(1 - \delta_{k0})\bar{a}_{kl}(1 - \langle n_{0\uparrow} \rangle)(1 - \langle n_{0\downarrow} \rangle) \\
&+ i\gamma_0\sqrt{2}\delta_{k0}a_{lk}(1 - \langle n_{0\uparrow} \rangle)(1 - \langle n_{0\downarrow} \rangle). \quad (13)
\end{aligned}$$

Note that the Hubbard interaction in this approximation is just a chemical potential for the holons and doublons, see Eq. (11), and therefore does not show up in the EOM's for these particles. The Hubbard interaction does, however, show up in the EOM's for the non-particle conserving, anomalous correlators which are given by

$$\begin{aligned}
i\dot{a}_{kl} &= -J(a_{k+1l} + a_{k-1l} + 2a_{kl+1} + 2a_{kl-1}) \\
&- \sqrt{2}J(d_{k-1l} + h_{l+1k} - \delta_{kl+1} - h_{l-1k} + \delta_{kl-1} - d_{k+1l}) \\
&- Ua_{kl} - i\gamma_0\sqrt{2}\delta_{k0}d_{kl}(1 - \langle n_{0\downarrow} \rangle)(1 - \langle n_{0\uparrow} \rangle) \\
&- i\gamma_0/2[\delta_{k0}a_{kl}(1 - \langle n_{0\uparrow} \rangle) + 3\delta_{l0}a_{kl}(1 - \langle n_{0\downarrow} \rangle)]. \quad (14)
\end{aligned}$$

The system of EOM's, Eqs. (12-14), can then be solved by numerical integration. Note that this approach is also a mean-field decoupling scheme—although different from the one discussed in Sec. II A 1—based on restricting the local Hilbert space to three states only and ignoring the infinite repulsion V between holons and doublons in Eq. (11) which is required to avoid unphysical states with a holon and a doublon occupying the same site. In the EOM's (12-14) this constraint is only implemented 'on average'.

B. LCRG and quantum trajectories

The quantum trajectory (QT) approach was developed in the 1990's^{22,23} as a wave-function approach to dissipative processes in quantum optics. The term quantum trajectories was coined by M. Carmichael.²³ Previously, it was called either the quantum jump approach or the Monte Carlo wave-function method. In general the QT approach can be used to solve any master equation in Lindblad form.³ An integration over these QT's can be carried out by any numerical approach that is able to solve the Schrödinger equation.

The main idea is to rewrite the master equation as a stochastic average of QT's. Each QT is dependent on random variables, thus no QT is identical in the limit time t to infinity. The main advantage of the QT approach is that only a quantum state has to be evolved in time thus avoiding to propagate the full density operator; only a Hilbert space with the dimension of the system

needs to be considered.^{3,22,23} The prize one has to pay is that many QT's (of the order of several hundred or even several thousand for the Bose-Hubbard model) have to be calculated to obtain meaningful averages. While memory requirements are reduced and obtainable simulation times often greatly enhanced as compared to a direct time evolution of the density matrix, the QT approach is therefore very costly in terms of computing time.

In previous studies of dissipative one-dimensional quantum systems, the QT approach has been combined with time-dependent DMRG algorithms for finite system size L^{10} and compared to the superoperator approach where the full density matrix is evolved in time.^{32,33} One problem with numerical algorithms for finite systems is that the only non-equilibrium steady state (NESS) which can be reached in a system with particle loss is the vacuum. We circumvent this problem here by combining the QT approach with the LCRG making it possible to discuss the physical properties at long times $t \gg J/\gamma$. The LCRG uses a Trotter-Suzuki decomposition of the time evolution operator³⁴ and the Lieb-Robinson bounds^{35,36} to restrict the time-evolution to an effective light cone for a Hamiltonian with short range interactions.²⁵ The LCRG algorithm efficiently simulates one-dimensional systems and yields observables directly in the thermodynamic limit.^{31,37,38} The Hilbert space is truncated based on the eigenvalues of the reduced density matrix following traditional DMRG schemes.^{15,17} Transfer matrices are used to enlarge and time-evolve the system stepwise. In an alternative description, a tensor network in matrix product state (MPS) language can be easily transformed to a light cone shape through this process, see Fig. 2.

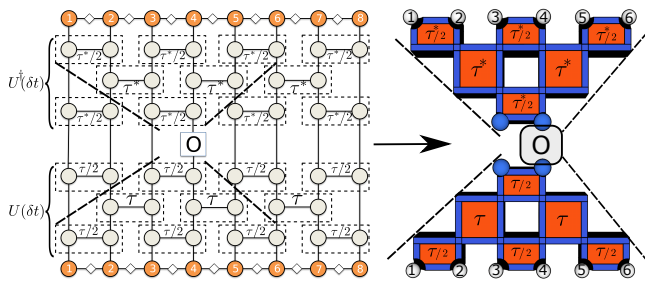


FIG. 2: Transformation from an MPS network after Trotter-Suzuki decomposition (left) to a light cone (right). The adjacent plaquettes outside the light cone, depicted by the black dotted line, cancel each other.

The aim of this section is to describe how to combine the LCRG with a QT scheme in order to generalize the LCRG algorithm to non-unitary time evolution in open systems for the special case where a single site is coupled to a bath. The LCRG keeps its light-cone shape for a non-unitary time-evolution carried out only locally. Translational invariance, however, is destroyed thus algorithms like the infinite TEBD^{39,40} cannot directly be applied to calculate the dynamics in the thermodynamic limit.

The size of the effective light cone in the LCRG algorithm at time t is given by

$$L = v_{\text{Trotter}}|t|, \quad v_{\text{Trotter}} = \frac{a}{\delta t}, \quad (15)$$

where v_{Trotter} is the Trotter speed and a the lattice constant which we have set to unity. It has been shown that for systems with short-range interactions the error between a time-dependent operator $\hat{O}_0^{(\ell)}(t)$ acting on the site $j = 0$ in the middle of an ℓ site light cone (see Fig. 2 and the operator $\hat{O}_0(t)$ evaluated in the infinite system is bounded by

$$\|[\hat{O}_0(t), \hat{O}_0^{(\ell)}(t)]\| \leq ce^{\left(-\frac{\ell - v_{\text{LR}}t}{\xi}\right)}, \quad (16)$$

where c is a constant, ξ the correlation length and v_{LR} the Lieb-Robinson velocity which is of order of the hopping amplitude J and describes the velocity information is spreading through the lattice.^{35,36} In the BHM the Lieb-Robinson bound has been observed in tDMRG simulations²⁹ and has also been verified in experiment.³⁰ In order to make the error in the LCRG simulations exponentially small as compared to results in the thermodynamic limit we therefore have to make sure that the condition $v_{\text{Trotter}} \gg v_{\text{LR}}$ is fulfilled. For the one-dimensional BHM in the limit of $U/J \rightarrow \infty$, doublon and holon excitations with velocities $v_{\text{doublon}} = 4J$ and $v_{\text{holon}} = 2J$ respectively exist.^{30,31} For a propagating doublon the Trotter time step therefore has to be chosen such that

$$1/\delta t \gg v_{\text{doublon}} \sim 4J. \quad (17)$$

In our simulations we usually set $J\delta t \sim 0.01$ or smaller, which obviously fulfills Eq. (17). We thus obtain results in the thermodynamic limit with the light-cone structure only introducing exponentially small errors.

The QT approach can then be combined with the LCRG algorithm in the following way: The system without dissipation evolves under a Hamiltonian $H = \sum_j h_{j,j+1}$. For a system with hopping terms or interactions beyond nearest-neighbors the unit cell has to be expanded accordingly. Adding local dissipation at site k we have to replace the local Hamiltonian by $h_{j,j+1} \rightarrow h_{j,j+1}^{\text{eff}} = h_{j,j+1} - \delta_{jk} \frac{\gamma k}{2} \hat{A}_k^\dagger \hat{A}_k$. The local time evolution operator in Trotter-Suzuki decomposition is then given by $\tau = \exp(-i\delta t h_{j,j+1}^{\text{eff}})$ and is depicted as a plaquette in Fig. 2. Next, we draw a random number $r \in [0, 1)$. The normalized initial state is now time-evolved $|\Psi(\delta t)\rangle = \exp(-iH^{\text{eff}}\delta t)|\Psi(0)\rangle$. If $r < \|\Psi(\delta t)\|$ we continue with the time evolution. If, on the other hand, $r \geq \|\Psi(\delta t)\|$ then we apply the local operator A_k onto the state, $|\Psi(\delta t)\rangle \rightarrow A_k|\Psi(\delta t)\rangle$, realizing a quantum jump. After the quantum jump the time evolved state is normalized, a new random variable $r \in [0, 1)$ is drawn, and the state is further evolved in time under the effective Hamiltonian until the next quantum jump occurs. In the implementation it is important to use very small time steps close the point where the quantum jump

occurs in order to avoid having many trajectories which jump at exactly the same time.^{10,33} For each QT the expectation value of the variable of interest is measured and then averaged over all QT's. The statistical error of an observable is simply given by $\sigma_A(\hat{O}) = \frac{\sigma(\hat{O})}{\sqrt{Q}}$, where Q is the number of QT and $\sigma(\hat{O})$ the standard deviation because the QT's are statistically independent.^{3,22} For the density and current profiles we typically need several hundred QT's to obtain statistical errors which are small compared to the dynamical changes of the observables. The number of states χ which we need to keep is adjusted dynamically so that the truncation error always stays below 10^{-7} . This typically requires the number of states to be in the range $\chi \sim 300 - 1850$ for the examples considered later. Furthermore, we always recompute each QT with a higher bond dimension to make sure that all QT's are converged as one fixed χ does not apply to all QT's.

C. Preparation of initial state and comparison with exact diagonalization

We consider dissipative dynamics starting from the ground state of the closed system. In order to compute the ground state within the LCRG scheme, imaginary time evolution is used. Because the Bose-Hubbard model lacks particle-hole symmetry, the correct chemical potential μ needs to be included in the imaginary time evolution operator

$$\tau_\beta = \exp \left\{ -\beta(H - \mu \sum_j n_j) \right\}. \quad (18)$$

Here β is imaginary time. The time evolution operator is then considered in Trotter-Suzuki composition and β successively increased to project an arbitrary initial state onto the ground state. In practice, we cannot reach the limit $\beta \rightarrow \infty$ so that the projection will not be exact. However, if there is a gap Δ_E between the ground state and the first excited state then the error will be exponentially small, $\sim \exp(-\beta\Delta_E)$, if $\beta\Delta_E \gg 1$.

As an example, we consider imaginary time evolution deep in the Mott-insulating phase for $U = 12J$. For $\beta \sim 5$, we find that the energy of the state is already converged. To further test the properties of the projected state, we consider the connected density-density correlation function

$$g^c(j, t) = \langle n_0 n_j \rangle(t) - \langle n_0 \rangle \langle n_j \rangle(t). \quad (19)$$

As shown in Fig. 3, the projected state is not a simple product state but rather shows the physically expected exponentially decaying correlations. We ensure that the energy is converged for all the projected ground states considered in the following and that the correlations are properly captured.

As a next step, we test the QT-LCRG algorithm by comparing results for the BHM with local particle loss

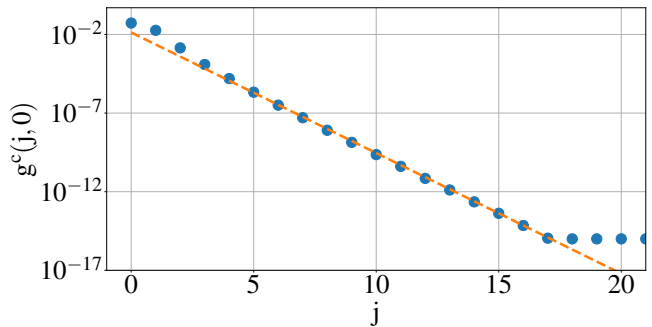


FIG. 3: Connected density-density correlation function, Eq. (19), in the projected state for $U = 12J$: $g^c(j, 0)$ is decaying exponentially with a correlation length $\xi \approx 0.57$. The line is an exponential fit. Correlations for $j > 17$ are of the order or smaller than 10^{-16} and are therefore not correctly reproduced in double precision.

with a solution of the Lindblad equation (3) based on exact diagonalizations (ED). Note that such a comparison is only meaningful for observables at or very close to the lossy site (which will always be in the middle of the considered chain) and small times because ED is limited to very small system sizes. In Fig. 4 results for the density $n_0(t)$ at the lossy site calculated with the QT-LCRG algorithm using 500 – 2000 QT's are compared to the ED result. Within the statistical errors, both results

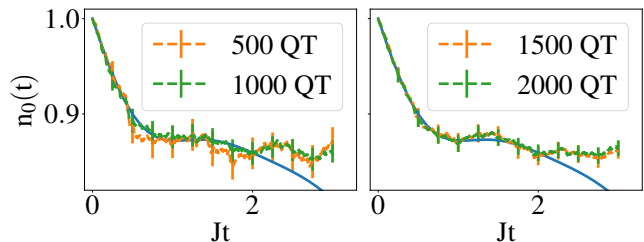


FIG. 4: Time evolution of the density $n_0(t)$ at the dissipative site starting from the Mott-insulating state with $U = 12J$. Compared are QT-LCRG results (error bars denote the statistical errors) with exact diagonalization data (solid line) for a chain of $L = 5$ sites and $\gamma = 0.25$. Boundary effects for $n_0(t)$ become visible in the ED results for $Jt \geq 2$.

agree for $Jt \leq 2$.

III. RESULTS

In the following, we want to analyze results obtained by the QT-LCRG algorithm for the density and current profiles, the density-density correlations, as well as the entanglement entropy. We will compare these results to the EOM approach and are, in particular, interested in the long-time regime where many-body effects dominate and the EOM approach in Hartree-Fock approximation is expected to fail. We will mainly concentrate on the

case of weak dissipation but will also briefly discuss the case of strong dissipation towards the end of this section.

A. Particle and density profiles

When a hole is created at the lossy site $j = 0$, this density perturbation starts to move through the lattice with the holon velocity which is approximately given by $v \sim 2J$ for $U/J \gg 1$. Based on the effective fermion model description, Eq. (11), we see that alternatively also a doublon can be annihilated—although the doublon density in the initial Mott insulating state with $\langle n_j \rangle = 1$ will be small—, creating a perturbation which will travel with twice the holon velocity.³¹ For small dissipation and large U we cannot reliably detect the doublon contribution numerically so that the density profile has a light cone structure at short times given by the holon velocity, see Fig. 5. However, the doublon contribution is present and can be detected numerically for larger γ values, see the inset of Fig. 5.

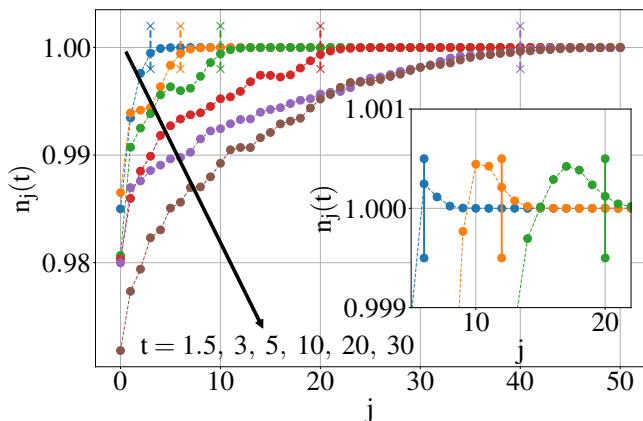


FIG. 5: Density profiles at short and intermediate times for $U = 12$ and $\gamma = 0.025$. The holons spread in a light-cone like fashion with the numerically calculated velocity $v \approx 2J$ (vertical bars).³¹ Averages over 2589 converged QT's for $t \leq 20$ and 1089 for $t > 20$ are shown for bond dimensions $\chi = 900 - 1450$. The statistical error is largest at the dissipative site, $\sigma_A^0 \approx 0.0028$. Inset: For $U = 12$, $\gamma = 8$ a doublon contribution is clearly visible with $v \approx 4J$ (vertical bars).

The changes of the density profiles are caused by local currents which can be calculated from the continuity equation $\langle \dot{n}_j \rangle = -\langle \text{div } \mathcal{J} \rangle = -(\langle \mathcal{J}_j \rangle - \langle \mathcal{J}_{j-1} \rangle)$ with

$$\begin{aligned} \dot{n}_j = \dot{\sigma}_{jj} &= iJ(\sigma_{j,j+1} - \sigma_{j+1,j} + \sigma_{j,j-1} - \sigma_{j-1,j}) \\ &\quad - \gamma_0 \delta_{j0} \sigma_{jj}, \end{aligned} \quad (20)$$

see Eq. (5). The local current operator originating from the unitary part is therefore given by

$$\mathcal{J}_j = -iJ \left(b_j^\dagger b_{j+1} - b_{j+1}^\dagger b_j \right). \quad (21)$$

Using the current operator, the change of the local density can also be written as

$$\frac{d}{dt} \langle n_j \rangle = \begin{cases} \langle \mathcal{J}_{j-1} \rangle - \langle \mathcal{J}_j \rangle - \gamma_0 \langle n_0 \rangle & i = 0 \\ \langle \mathcal{J}_{j-1} \rangle - \langle \mathcal{J}_j \rangle & \text{else} \end{cases} \quad (22)$$

with $\langle \mathcal{J}_j \rangle = 2 \text{Im} \langle b_j^\dagger b_{j+1} \rangle$. At short times inside the light cone we expect that $\frac{d}{dt} \langle n_j \rangle < 0$ which is equivalent to $\langle \mathcal{J}_j \rangle > \langle \mathcal{J}_{j-1} \rangle$ for $|j| > 1$. For $j > 1$ (to the right of the dissipative site) at the boundary of the light-cone we expect $0 \approx |\langle \mathcal{J}_j \rangle| < |\langle \mathcal{J}_{j-1} \rangle|$ which implies that the currents are negative, i.e., are pointing towards the dissipative site. As long as the local densities inside the light cone are decreasing we furthermore expect that the local currents $\langle \mathcal{J}_{j>0} \rangle$ are a monotonically increasing function of the distance j from the dissipative site. Because the Hamiltonian is reflection symmetric around $j = 0$ there is always a current equal and opposite in direction on the other side of the lossy site

$$\langle \mathcal{J}_j \rangle(t) = -\langle \mathcal{J}_{-j-1} \rangle(t). \quad (23)$$

Furthermore, we can also immediately read off the stationary current from Eq. (22) by demanding $\frac{d}{dt} \langle n_j \rangle = 0$ for all sites j . Using Eq. (23) this leads to

$$\langle \mathcal{J}_j \rangle_{\text{NESS}} = \begin{cases} -\gamma_0 \langle n_0 \rangle / 2 & j \geq 0 \\ \gamma_0 \langle n_0 \rangle / 2 & j < 0 \end{cases}. \quad (24)$$

At short times our numerical results for the currents are consistent with these considerations, see Fig. 6. We

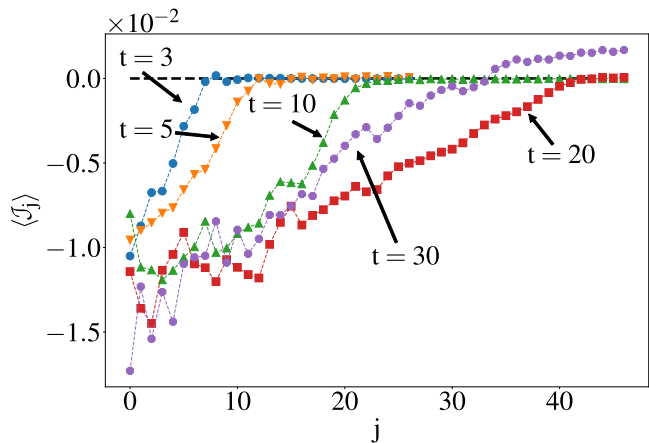


FIG. 6: Current profiles at short and intermediate times for $U = 12$ and $\gamma = 0.025$ with 1500 converged QT's for $t \leq 20$ and 574 for $t > 20$. At times $t > 20$ a current reversal at sites far away from the lossy site is starting.

have also checked that the density and current profiles are consistent with the continuity equation (22). For intermediate times we find that the area of reduced density first continues to spread before essentially stopping to extend further at times $t \sim 30$. As shown in Fig. 5 the density at this point is significantly reduced on the first ~ 40 lattice sites around the defect. The current profiles shown in Fig. 6 also show an intricate evolution at this timescale. For the ~ 10 sites closest to the defect the currents, on average, stop growing for $t \geq 10$.

Even more remarkable, a local current reversal starts to set in for times $t > 20$ at sites further away from the defect. For time $t = 30$, for example, sites $j > 35$ have a local current *leading away* from the lossy site. This current reversal will ultimately reduce the area over which the density is significantly depleted while even further reducing the density close to the defect.

This effect can clearly be seen in the density profiles at the longest simulation times shown in Fig. 7. The densi-

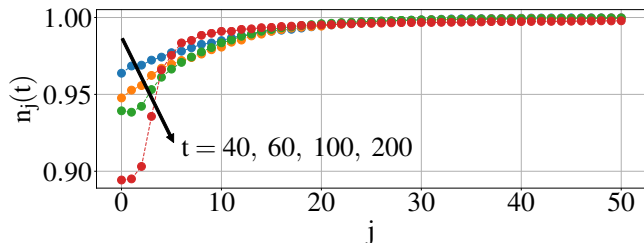


FIG. 7: Density profiles at long times for $U = 12$ and $\gamma = 0.025$. The density profile at sites $j \gtrsim 10$ changes only very little over time.

ties at sites $j \gtrsim 10$ only change very little in time while the densities at the sites closest to the defect continue to be reduced. The absolute values of the currents near the defect also do decrease at long times as shown in Fig. 8. Interestingly, all local currents for $j > 5$ are reversed at

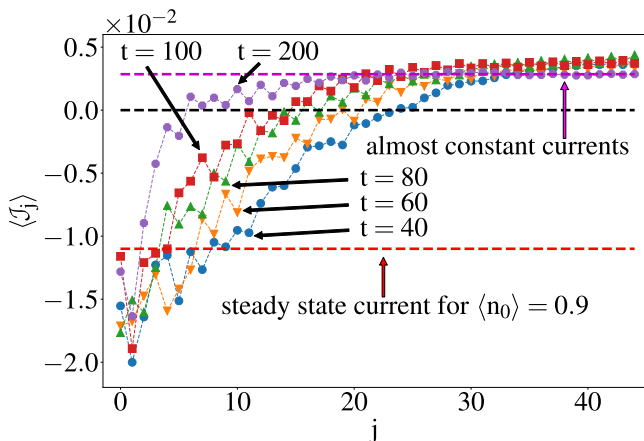


FIG. 8: Current profiles at long times for $U = 12$ and $\gamma = 0.025$. The local currents at $t = 200$ are reversed and are pointing away from the lossy site.

$t = 200$ and are flowing away from the defect. While the local currents are almost all equal as is expected in the steady state, see Eq. (24), the currents are flowing in the opposite direction than the steady state currents. Furthermore, the magnitude of the currents is much smaller than the steady state current for $\langle n_0 \rangle(t = 200) \approx 0.9$, see Fig. 8. We conclude that while the density profile appears to become almost independent of time and the local currents almost all equal to each other we are *not* in the non-equilibrium steady state of the system. The local

densities for times $t \in [150, 200]$, however, only change very little (see Fig. 9) indicating that we have reached a metastable steady state with small local currents pointing away from the lossy site. While the densities at sites

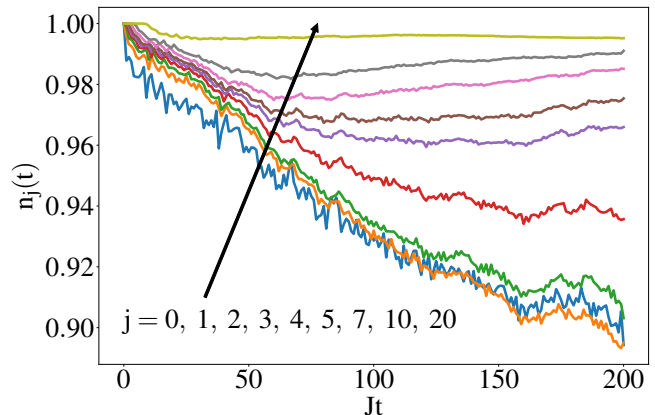


FIG. 9: Local densities as a function of time for weak local particle loss $\gamma = 0.025$. The local densities change very little in the time interval $t \in [150, 200]$ pointing to a metastable steady state.

$j = 0 - 3$ at times $t \in [150, 200]$ appear to be constant on average, the particle densities at sites $j = 5 - 10$ are monotonously but very slowly increasing. Even further away from the defect, on the other hand, the densities continue to decrease slowly.

While we cannot reach the non-equilibrium steady state, a likely scenario based on the density and current profiles is a steady state density profile which is quite steep with a density at the dissipative site which is strongly reduced—and perhaps much closer to zero than to 1—while substantial particle densities persist on all other sites. A small density at the dissipative site in the steady state would, according to Eq. (24), also lead to a small steady state current. The local currents at times $t > 200$ therefore possibly stay almost equal except very close to the dissipative site but slowly change sign again. Another surprising result of the simulations is the very large time scale apparently required to reach the NESS. One relevant time scale is clearly set by $J/\gamma = 40$ for the example considered here. In Fig. 9 this time scale separates the regime where the densities of sites inside the light cone change approximately linearly in time from a regime where the densities at some sites become already approximately constant or even start to slowly increase again. J/γ is also the time scale where some of the local currents start to reverse. In order to check this interpretation we also briefly consider the case $\gamma = 0.1$ in the following. In this case the local densities $\langle n_j \rangle(t)$ inside the light cone show an initial decay followed by a plateau around $J/\gamma = 10$ and then a further decay, see Fig. 10. Again, the time scale to reach the NESS appears to be much larger than J/γ .

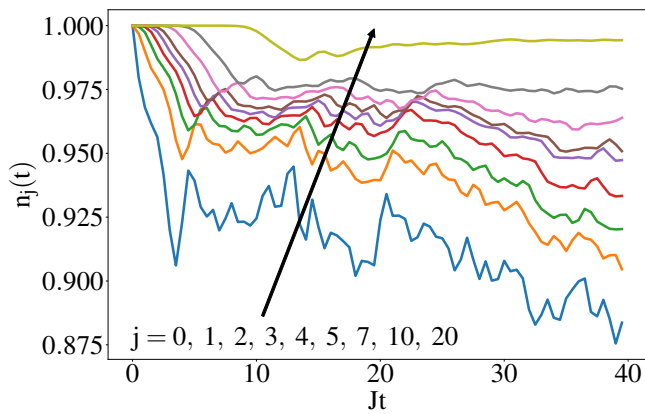


FIG. 10: Local densities as a function of time for $U = 12$ and $\gamma = 0.1$. Averages over 800 QT's are shown. At the time scale $J/\gamma = 10$ a plateau-like feature is visible.

B. Comparison with EOM

Next, we want to investigate how much of the complicated dynamics is captured in an EOM approach with a Hartree-Fock decoupling or within the effective fermion model approach, see Sec. II A. In Fig. 11 the density and current profiles obtained by LCRG and the first order Hartree-Fock EOM approach for short and intermediate times are compared. As initial state in the EOM calculations we use a product state with one boson per site which is a good approximation for the ground state at $U = 12$. While the density profiles for times $t = 5$ and

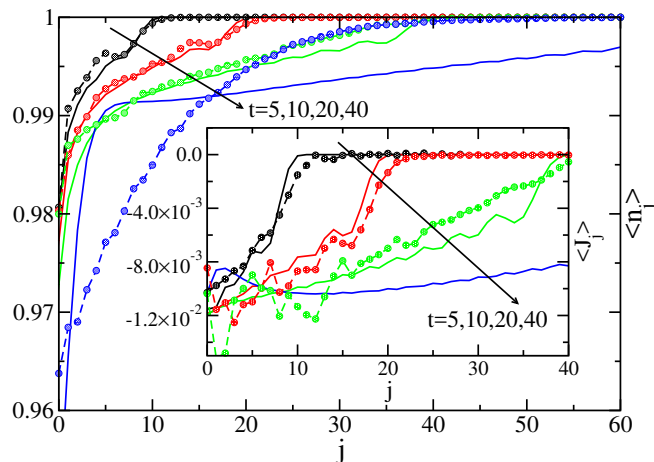


FIG. 11: Comparison of density profiles (main) and current profiles (inset) obtained by LCRG (symbols) and the EOM with Hartree-Fock decoupling (lines), see Eq. (5, 6), for $U = 12$ and $\gamma = 0.025$. LCRG current profiles are shown for $t = 5, 10, 20$ only for clarity.

$t = 10$ obtained by this mean-field EOM approach agree very well with the LCRG results, first significant deviations become visible at $t = 20$ and already at $t = 40$ the Hartree-Fock EOM approach fails completely. While

the LCRG data show that between time $t = 20$ and time $t = 40$ the densities at sites $j \geq 20$ no longer decrease, the EOM predicts a ballistic extension of the region with reduced particle density with the holon velocity $v \sim 2J$. That the EOM fails to capture essential aspects of the dynamics is also obvious from the current profiles shown in the inset of Fig. 11. While the current profiles are correctly captured for $t < 20$, the EOM approach completely fails for longer times (see also Fig. 8). In particular, current reversals away from the lossy site do not occur in the mean-field EOM solution. We conclude that the current reversals observed in the LCRG simulations are a genuine many-body effect which cannot be captured in a Hartree-Fock decoupling scheme. The Hartree-Fock solution—which is essentially the result for a Gaussian system—is only able to describe the initial dynamics at times $t < J/\gamma$.

The failure of the first order Hartree-Fock EOM decoupling scheme at long times raises the question if a different EOM scheme can better describe the system. We checked first that going to a second order scheme as described by Eqs. (7, 8) does not lead to any significant improvement but rather introduces instabilities at large U (data not shown). Another alternative is the EOM scheme for the effective fermion model derived in section II A 2. The potential advantage of this approach is that its starting point is the opposite limit of large U where the local Hilbert space can be limited to 3 states only. This approach does, however, have another problem: holons and doublons are allowed to occupy the same site at the same time because the hard-core constraint is an interaction between these particles which cannot be fully treated. For $U = 12$ and $\gamma = 0.025$ we find that the error induced in the current and density profiles by these unphysical states makes the results of the effective fermion model approach quantitatively unreliable, see Fig. 12. Nevertheless, these results show some interesting features which are not present in the Hartree-Fock approach. As the main qualitative difference we note that in the effective fermion model a doublon peak with local densities $\langle n_j \rangle > 1$ is clearly visible in the density profile. In the LCRG data such a doublon contribution also exists, but is much smaller. We have already shown in Fig. 5 that this contribution can be seen very clearly numerically at larger γ .

The local current operator, Eq. (21), in the effective fermion model is given by

$$\mathcal{J}_j = 2\mathcal{J}_j^\uparrow + \mathcal{J}_j^\downarrow \quad (25)$$

with the doublon and holon currents $\mathcal{J}_j^\sigma = -i\sigma J(c_{j,\sigma}^\dagger c_{j+1,\sigma} - c_{j+1,\sigma}^\dagger c_{j,\sigma})$ with $\sigma = \uparrow, \downarrow = +, -$. The Hamiltonian (11) of the effective fermionic model does contain doublon-holon pair creation and annihilation terms. In a short-time density profile, holes are spread in a light cone around the dissipative site. If a doublon excitation is now created on top of this profile it will have an enhanced probability to recombine

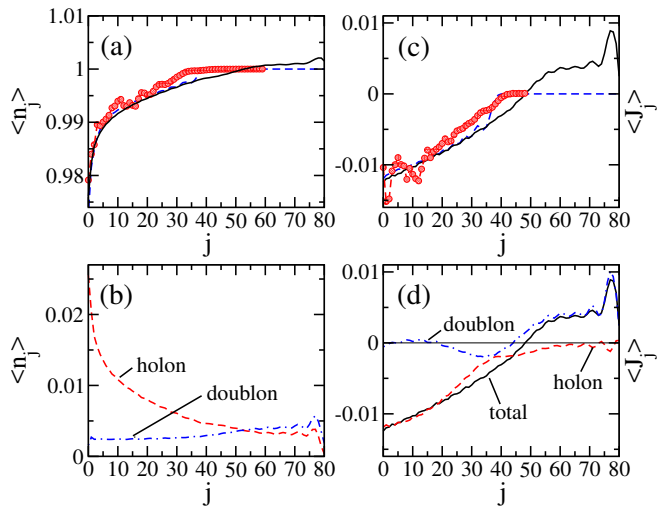


FIG. 12: (a) Density profiles from QT-LCRG (symbols), Hartree-Fock EOM (dashed line) and effective fermion model (solid line) at $t = 20$. (b) Density of holons and doublons at $t = 20$ in the EFM approach. (c,d) Same as (a,b) for the local currents.

with a hole if it travels towards the dissipative site while traveling away from the defect it has a higher probability to survive and travel on ballistically. We therefore expect that a *positive* doublon current $\langle \mathcal{J}_j^\uparrow \rangle$ is associated with the doublon peak seen in the density profiles in regions where the holon density is low. Such positive local currents are indeed seen in the numerical solutions of the EOM's for the effective fermion model, see Fig. 12(c,d). The EFM therefore seems to be able to qualitatively explain the onset of local current reversals far from the dissipative site: while the local currents close to the defect are dominated by the holon current \mathcal{J}_j^\downarrow , the faster doublon excitation can move ballistically on a background without holes outside the holon light cone leading to small local currents which are positive. This is—in a loose sense—reminiscent of Hawking radiation where particle-antiparticle pairs are created close to the event horizon with one particle falling back into the black hole while the other escapes. In our system there is, however, no sharp horizon between the region of reduced density and the 'vacuum' ($\langle n_j \rangle = 1$) and the energies of the escaping doublons will not show a thermal distribution. The system is not a sonic analog of a gravitational black hole. We further note that the EFM model is not able to describe the metastable state in which all local currents are reversed. It also always overestimates the doublon contribution because the doublons can travel on top of the holons in the approximation considered here.

C. Particle loss

The particles lost at the defect can be detected, for example, in a cold gas experiment where an electron beam is used to ionize atoms. The ions then leave the trap and are collected by a detector.⁶ In the QT approach each quantum jump corresponds to a particle which is removed from the system. The total number of particles lost at a given time t can therefore be calculated by counting the quantum jumps,

$$N(t) = \lim_{Q \rightarrow \infty} \frac{1}{Q} \sum_{i=1}^Q \int_0^t \delta(t' - t_{\text{jump}_i}) dt', \quad (26)$$

where Q is the number of QT's. Experimentally, the quantum jumps for a single QT correspond to a possible timeline of detection events. The average particle loss rate $\dot{N}(t)$ has to become a constant in the NESS. For an infinite system, it is important to distinguish the particle loss, Eq. (26), measured by a detector from the overall change of the density profile

$$D(t) = \sum_{l=-\infty}^{\infty} n_l(t=0) - n_l(t), \quad (27)$$

seen, for example, by in-situ imaging. While $D(t)$ and $N(t)$ are identical for a finite system, this is no longer the case if an infinite reservoir of particles exists. For the infinite system we expect a non-trivial time-independent density profile $D_\infty = D(t \rightarrow \infty)$ in the NESS.

In Fig. 13 we show LCRG results for $N(t)$ and $D(t)$. At

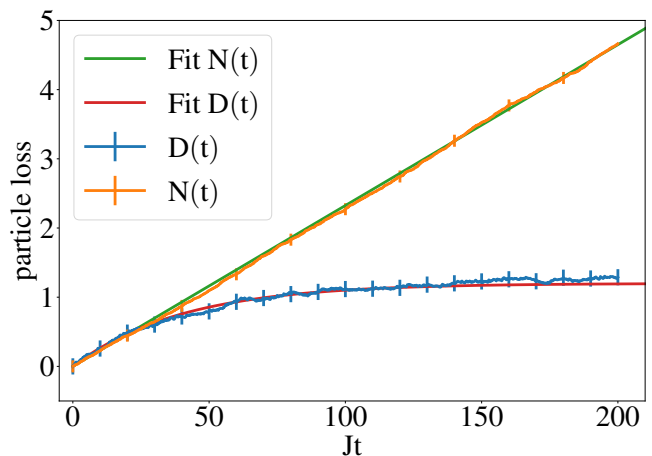


FIG. 13: Particle loss $N(t)$ and overall change of the density profile $D(t)$ for $U = 12$ and $\gamma = 0.025$. The lines are fits, see text.

short times $D(t) \approx N(t)$ but at times $t \gtrsim 20$ both start to deviate. Note that this is roughly the time scale where the region of reduced particle density stops to extend ballistically with the holon velocity $v \sim 2J$, see Fig. 5. The change in the density profile can be well approximated by

$$D(t) \sim A(1 - e^{-\gamma t}), \quad (28)$$

with γ being the dissipation rate as has also been observed previously in Ref.10. This seems to suggest that the time scale for reaching the steady state is $\sim J/\gamma$. It is important to stress once more, that this is not the case. Our simulations show that the density profile continues to change substantially for times $t \gg J/\gamma$. The continuing density reduction at sites close to the defect is, however, largely compensated for by a refilling of sites further away from the defect, making $D(t)$ almost constant for $t > J/\gamma$. The short time expansion, $D(t) \approx A\gamma t$ does not only capture the behavior of $D(t)$ at times $t \lesssim 20$ but also yields a good approximation for the particle loss rate $\dot{N}(t) \sim A\gamma$. Within error bars, $\dot{N}(t)$ does not change as a function of time and is therefore not a useful quantity to detect whether or not the NESS has been reached.

In Fig. 14 the constant rate $\dot{N}(\gamma, t \gg J/\gamma)$ is shown as a function of the dissipation strength γ . The loss

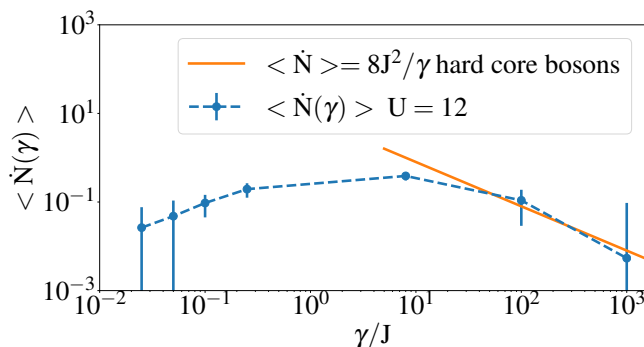


FIG. 14: Particle loss rate $\dot{N}(\gamma, t \gg J/\gamma)$ for $U = 12$ as a function of dissipation strength γ . The error bars denote the corresponding statistical errors. For large dissipation, the numerical results are well described by the perturbative result $\dot{N}(\gamma, t \gg J/\gamma) = 8\gamma^2/J$.

rate goes through a maximum at $\gamma/J \approx 8$ before falling off of $\sim \gamma^2/J$ for large dissipation strengths.¹¹ This counterintuitive effect is known as quantum Zeno dynamics. Large dissipation strengths effectively stabilize configurations at long times where the dissipative site is unoccupied with $\gamma \gg J$ effectively acting as a potential barrier strongly reducing the hopping onto the lossy site. Our results for the loss rate are consistent with previous numerical and experimental studies.^{6,10,11}

D. Long-range correlations

The quench dynamics we are investigating here starts from a ground state deep inside the Mott insulating phase. This state has exponentially decaying density-density correlations with a rather small correlation length of about half a lattice site, see Fig. 3. Here we want to study how these correlations change once the dissipative dynamics sets in. We concentrate on the connected equal

time density-density correlation function between the dissipative site and other sites in the lattice, see Eq. (19).

At short times, the density perturbation created by turning on the dissipative process at site $j = 0$ at time $t = 0$ travels with the holon velocity $v \sim 2J$ through the system creating a light cone, see Fig. 15. While this den-

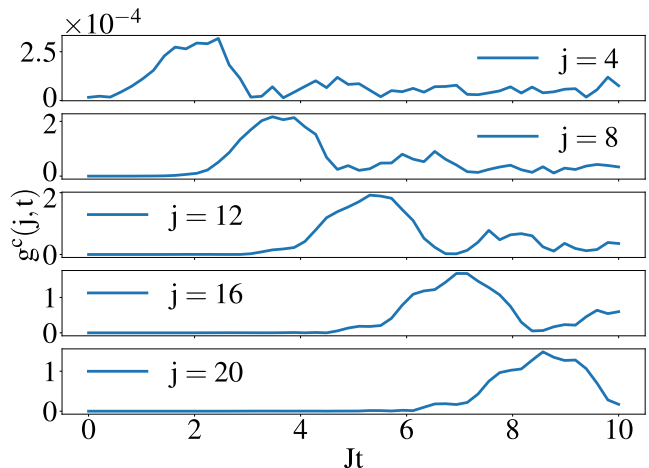


FIG. 15: QT-LCRG data for the time-evolution of $g^c(j, t)$ at selected sites of the chain for $U = 12$ and $\gamma = 0.025$. A density wave propagates through the chain with velocity $v \approx 2J$.

sity wave travels through the chain, it leaves behind sites which are stronger correlated than in the initial state. Fig. 16 shows that the correlations between the lossy site and sites inside the holon light cone for times ≤ 10 even appear to be long-ranged. Obtaining accurate data for

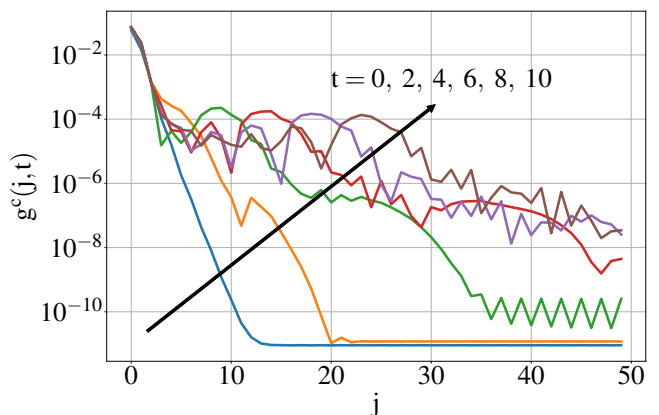


FIG. 16: The spatial profile of $g^c(j, t)$ at selected times starting from a Mott-insulating ground state at $U = 12$. At time $t = 0$ the correlations decay exponentially with $\xi \approx 0.57$. The weak dissipative defect induces correlations inside the holon light cone which are much longer ranged. The maximal error of the data is of the order $\sim 10^{-6}$.

the density-density correlation function requires to calculate ~ 10000 QT's which is computationally very demanding. The data in Fig. 16 are therefore limited to short times. Based on these data it is impossible to ana-

lyze in more detail if truly long-ranged, power-law decaying, or exponentially decaying correlations with a large correlation length are established.

E. Initial conditions and NESS

In Ref.8 a BHM with local particle loss was studied. The experiment showed a bistability in a certain parameter regime: different steady states are reached depending on whether or not the lossy site has the same filling as the other sites or is empty in the initial state. In contrast to our study, the experiment was performed in the superfluid regime with each site occupied on average by several hundred bosons.

In the following we will investigate if a similar bistability also exists deep in the Mott insulating phase. Similar to the experiment, we modify the density $\langle n_0 \rangle$ in the Mott-insulating initial state. In Fig. 17(a) we show results for the evolution of $\langle n_0(t) \rangle$ obtained using the Hartree-Fock EOM approximation for initial states with densities $\langle n_0(0) \rangle \in [0, 1]$. Interestingly, the results indeed

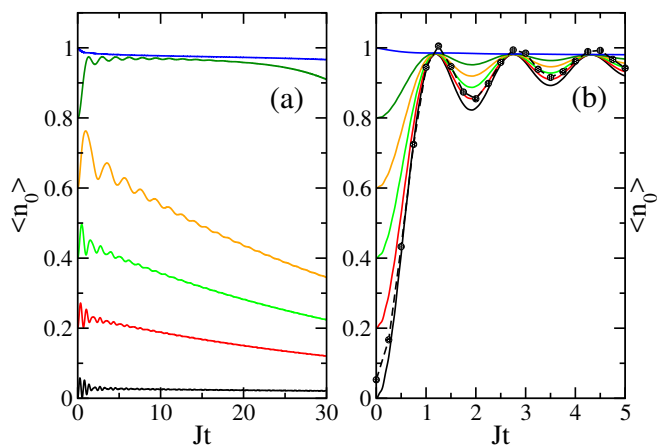


FIG. 17: Time evolution of the density at the lossy site for initial states with different fillings of the lossy site for $U = 12$ and $\gamma = 0.025$. (a) Results of the Hartree-Fock EOM approximation do show a bistability. (b) No bistability is seen using the EOM's for the EFM. The result for initial filling $\langle n_0 \rangle \approx 0$ is in good agreement with the QT-LCRG data (dots).

point to a bistability where the site n_0 becomes almost completely empty or refills almost completely at intermediate times with a critical filling $\langle n_0^{\text{crit}}(0) \rangle \sim 0.7$. The results obtained using the EOM's for the effective fermion model are shown in Fig. 17(b) and are very different from the Hartree-Fock approximation. For all initial states the site n_0 fills up again over a rather short time scale. There is no bistability. The results for initial filling $\langle n_0 \rangle = 0$ for the effective fermion model are consistent with QT-LCRG data, see symbols in Fig. 17(b). Note that the initial states in the two approaches are slightly different: We solve the EOM's for an initial product state with

$\langle n_0 \rangle = 0$ and $\langle n_j \rangle = 1$ for all other sites. In the QT-LCRG calculations, on the other hand, we first calculate the ground state $|\Psi_0\rangle$ at $U = 12$. We then obtain the initial state as $b_0|\Psi_0\rangle$. Because $|\Psi_0\rangle$ is not a product state, part of the density is removed from neighboring sites and $\langle n_0 \rangle \approx 0.05$ in the initial state.

While the Hartree-Fock and the EFM approach yield similar results at short times if we start from the initial state with $\langle n_j \rangle = 1$ at all sites, only the EFM approach is able to describe the short-time dynamics properly if we start with a reduced density at the lossy site. This underlines that the EFM approach does capture the essential aspects of the short-time dynamics and is a good basis to qualitatively understand the properties of the system deep in the Mott-insulating phase. We also note that we have only studied one particular loss rate, $\gamma = 0.025$, here. Investigating whether or not bistabilities do occur in the Mott-insulating initial state for larger loss rates is beyond the scope of this study.

F. Entanglement entropy

The QT-LCRG algorithm is based on approximating the time-evolved state as a matrix product. The success of such an approach hinges on the amount of entanglement entropy produced by the time evolution. The Hilbert space is truncated using a reduced density matrix $\rho_{\text{red}} = \text{tr}_E \rho$ where ρ is the full density matrix and E the part of the system which is traced out. The entanglement entropy is then given by

$$S_{\text{ent}} = -\text{tr}\{\rho_{\text{red}} \ln \rho_{\text{red}}\} \quad (29)$$

and is bounded by $\ln \chi$ where χ is the dimension of ρ_{red} . Since the matrix dimensions which can be handled numerically is limited in practice, only states with $S_{\text{ent}} \ll \ln \chi$ can be faithfully represented.⁴¹ It is therefore interesting to study the time evolution of the entanglement entropy for the lossy BHM.

In the QT approach, $S_{\text{ent}}(t)$ will be different for each trajectory. In order to simulate the time evolution we have to keep a sufficient number of states χ such that the entropy for the QT's with the most entanglement always remains small compared to $\ln \chi$. In the following, we will concentrate on the entanglement entropy S_{ent}^0 obtained by tracing out all sites in the density matrix to the right of the lossy site $j = 0$. Note that the system is not translationally invariant. In the algorithm we also need the reduced density matrix where all sites to the right of $j = 1$ are traced out. For small loss rates the entropies for both matrices are, however, similar so that it suffices to consider S_{ent}^0 here. In Fig. 18 the maximal, minimal, and the entropy averaged over all QT's are shown for $\gamma = 0.025$ and $\gamma = 0.1$. Quantum jumps typically lead to an abrupt increase of the entanglement entropy. Trajectories therefore exist which already have significant entanglement at short times. The imaginary

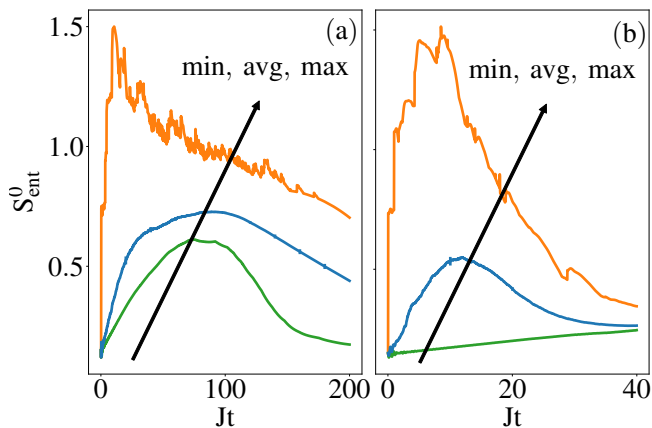


FIG. 18: Entanglement entropy S_{ent}^0 for $U = 12$ and (a) $\gamma = 0.025$, (b) $\gamma = 0.1$.

part of the effective Hamiltonian, on the other hand, suppresses entanglement. At short and intermediate times, the trajectory with the minimal entanglement is the one which contains no quantum jumps, while the trajectory with the maximal entanglement contains many jumps. At long times the two curves for the extrema apparently converge, pointing to a NESS or metastable state which has low entanglement. The average entanglement entropy first shows an approximately logarithmic growth, reaches a maximum, and then starts dropping almost linearly. For the simulations this means that one has to keep sufficient states to overcome the maximum in the entanglement entropy at intermediate times. The simulation time is then not restricted by a growing S_{ent}^0 —as is typically the case for quenches in closed quantum systems—but rather by the number of renormalization group steps which can be performed before the accumulated truncation error leads to a breakdown. For small dissipation rates the QT-LCRG is therefore an attractive tool to investigate the long-time dynamics of infinite one-dimensional quantum systems.

IV. CONCLUSIONS

Using a novel algorithm which combines the quantum trajectory approach with the lightcone renormalization group, we have investigated the dynamics of the Bose-Hubbard model at long-times, $t \gg J/\gamma$. Starting from a Mott-insulating initial state we found that for weak particle loss, $\gamma \ll J \ll U$, an intriguing long-time dynamics takes place.

Counterintuitively, a reversal of local currents sets in at times $t \sim J/\gamma$ leading to a state where almost all local currents are equal and pointing *away* from the lossy site. We argued that this state cannot be the steady state but rather is an unusual metastable state. In the steady state, all currents are equal and are pointing *towards* the lossy site. The currents therefore have to reverse again at

longer times. The reversal of local currents at intermediate times at sites outside the region with substantially reduced particle density can be qualitatively understood in an effective fermion description. In this approach the local Hilbert space is restricted to three states: empty (holon), singly occupied (vacuum), and doubly occupied (doublon). While fermionizing the model discards unphysical states with more than one holon or more than one doublon per site, doublon and holon can still occupy the same site. While these unphysical states mean that this approach is quantitatively not fully reliable, it does explain the qualitative features of the dynamics seen in the numerical simulations. The Bose-Hubbard Hamiltonian in the effective fermion representation contains terms annihilating or creating holon-doublon pairs on neighboring sites. For a pair created near the edge of the region with reduced density, in particular, the holon has an advanced probability to move towards the lossy site while the doublon is more likely to escape. The process is—in a loose sense—reminiscent of Hawking radiation near the event horizon of a black hole and leads to local currents which are pointing away from the dissipative site.

For a system with infinite particle reservoirs as considered here it is important to distinguish between the density loss as measured by a detector and the overall change of the density profile. While the former is a linear function of time with constant slope for all times and is therefore not useful to detect whether or not the system has reached the steady state, the latter exponentially slowly approaches a constant with a rate $\sim \gamma$. However, this does not imply that the steady state is reached on time scales $\sim J/\gamma$. The density profile continues to change substantially at times $t > J/\gamma$ with a density loss at sites close to the defect almost compensated for by a refilling of sites further away from the defect.

In the density-density correlations at short times a light cone structure is clearly visible. Once the front of the light cone has passed, correlations between the dissipative site and sites inside the cone are established which are much longer ranged than in the initial Mott-insulating state. An interesting question is if the dissipative dynamics can create truly long-range correlations. Numerically, this question is very difficult to address because a large number of trajectories are required to obtain reliable results for two-point correlation functions. Based on the data for times $Jt < 10$ we cannot decide if the correlations are truly long-ranged, power-law decaying, or even exponentially decaying with a very long correlation length.

Starting from initial states with different initial filling of the dissipative site we studied if the Lindblad dynamics can lead to different steady or metastable states. While the Hartree-Fock equation of motion approach suggests a bistability, similar to the one seen in a cold gas experiment in the superfluid regime, such a behavior is not confirmed in the effective fermion model. For the small dissipation rate γ considered, all initial states with dif-

ferent filling of the lossy site seem to lead to the same steady state. We showed, in particular, that the numerically calculated dynamics starting from the state where the lossy site is initially empty is in good agreement with the effective fermion model result. This underlines that the effective fermion model is a useful approach to understand the qualitative features of the open Bose-Hubbard dynamics at short and intermediate times deep inside the Mott-insulating regime.

The chosen model and parameters can be realized in a cold gas experiment. Detecting the doublons moving away from the dissipative site would be an indicator for the separation of holon-doublon pairs by the dissipation. While the considered system does not have a sharp event horizon, studying particles expelled from the dissipative region might be a step towards realizing sonic analogs of gravitational black holes. In order to achieve a full analogy, local losses in Bose gases in the superfluid phase

in higher dimensions need to be realized.⁴² Such systems are, however, more difficult to analyze theoretically beyond the mean-field level so that a careful study of losses in one-dimensional lattice models might be a useful interim goal.

Acknowledgments

We acknowledge support by the Natural Sciences and Engineering Research Council (NSERC, Canada) and by the Deutsche Forschungsgemeinschaft (DFG) via Research Unit FOR 2316. We are grateful for the computing resources provided by Compute Canada and Westgrid as well as for the GPU unit made available by NVIDIA. J.S. acknowledges helpful discussions with J. Anglin, M. Fleischhauer, and H. Ott.

-
- ¹ I. Bloch, Nat. Phys. **1**, 23 (2005).
² T. Tomita, S. Nakajima, I. Danshita, Y. Takasu, and Y. Takahashi, arXiv:1705.09942 (2017).
³ A. J. Daley, Advances in Physics **63**, 77 (2014).
⁴ F. Verstraete, M. M. Wolf, and J. Ignacio Cirac, Nat. Phys. **5**, 633 (2009).
⁵ N. Syassen, D. M. Bauer, M. Lettner, T. Volz, D. Dietze, J. J. García-Ripoll, J. I. Cirac, G. Rempe, and S. Dürr, Science **320**, 1329 (2008).
⁶ G. Barontini, R. Labouvie, F. Stubenrauch, A. Vogler, V. Guarrera, and H. Ott, Phys. Rev. Lett. **110**, 035302 (2013).
⁷ R. Labouvie, B. Santra, S. Heun, S. Wimberger, and H. Ott, Phys. Rev. Lett. **115**, 050601 (2015).
⁸ R. Labouvie, B. Santra, S. Heun, and H. Ott, Phys. Rev. Lett. **116**, 235302 (2016).
⁹ K. V. Keesidis and M. J. Hartmann, Phys. Rev. A **85**, 063620 (2012).
¹⁰ P. Barmettler and C. Kollath, Phys. Rev. A **84**, 041606 (2011).
¹¹ J. J. García-Ripoll, S. Dürr, N. Syassen, D. M. Bauer, M. Lettner, G. Rempe, and J. I. Cirac, New Journal of Physics **11**, 013053 (2009).
¹² A. J. Daley, J. M. Taylor, S. Diehl, M. Baranov, and P. Zoller, Phys. Rev. Lett. **102**, 040402 (2009).
¹³ E. P. van Nieuwenburg, J. Y. Mal, A. J. Daley, and M. H. Fischer, arXiv:1706.00788 (2017).
¹⁴ J.-S. Bernier, R. Tan, L. Bonnes, C. Guo, D. Poletti, and C. Kollath, arXiv:1702.04136 (2017).
¹⁵ S. R. White, Phys. Rev. Lett. **69**, 2863 (1992).
¹⁶ A. J. Daley, C. Kollath, U. Schollwöck, and G. Vidal, J. Stat. Mech. P04005 (2004).
¹⁷ S. White and A. E. Feiguin, Phys. Rev. Lett. **93**, 076401 (2004).
¹⁸ G. Vidal, Phys. Rev. Lett. **91**, 147902 (2003).
¹⁹ M. Zwolak and G. Vidal, Phys. Rev. Lett. **93**, 207205 (2004).
²⁰ F. Verstraete, J. J. García-Ripoll, and J. I. Cirac, Phys. Rev. Lett. **93**, 207204 (2004).
²¹ K. Macieszczak, M. Guță, I. Lesanovsky, and J. P. Garrahan, Phys. Rev. Lett. **116**, 240404 (2016).
²² K. Mølmer, **10**, 524 (1993).
²³ H. J. Carmichael, Springer, Berlin (1993).
²⁴ H.-P. Breuer and F. Petruccione, Oxford University Press (2002).
²⁵ T. Enss and J. Sirker, New J. Phys. **14**, 023008 (2012).
²⁶ P. Würtz, T. Langen, T. Gericke, A. Koglbauer, and H. Ott, Phys. Rev. Lett. **103**, 080404 (2009).
²⁷ G. Kordas, D. Witthaut, P. Buonsante, A. Vezzani, R. Burioni, A. I. Karanikas, and S. Wimberger, Eur. Phys. J. Special Topics **224**, 2127 (2015).
²⁸ G. Kordas, D. Witthaut, and S. Wimberger, Ann. Phys. (Berlin) **527**, 619 (2015).
²⁹ P. Barmettler, D. Poletti, M. Cheneau, and C. Kollath, Phys. Rev. A **85**, 053625 (2012).
³⁰ Marc Cheneau, Peter Barmettler *et al.*, Nature **481**, 484 (2012).
³¹ F. Andraschko and J. Sirker, Phys. Rev. B **91**, 235132 (2015).
³² L. Bonnes, D. Charrier, and A. M. Läuchli, Phys. Rev. A **90**, 033612 (2014).
³³ L. Bonnes and A. Läuchli, arXiv:1411.4831 (2014).
³⁴ M. Suzuki, Commun. Math. Phys. **51**, 183 (1976).
³⁵ E. H. Lieb and D. W. Robinson, Commun. Math. Phys. **28**, 251 (1972).
³⁶ S. Bravyi, M. B. Hastings, and F. Verstraete, Phys. Rev. Lett. **97**, 050401 (2006).
³⁷ F. Andraschko, T. Enss, and J. Sirker, Phys. Rev. Lett. **113**, 217201 (2014).
³⁸ T. Enss, F. Andraschko, and J. Sirker, Phys. Rev. B **95**, 045121 (2017).
³⁹ G. Vidal, Phys. Rev. Lett. **98**, 070201 (2007).
⁴⁰ R. Orús and G. Vidal, Phys. Rev. B **78**, 155117 (2008).
⁴¹ F. Verstraete and J. I. Cirac, Phys. Rev. B **73**, 094423 (2006).
⁴² L. Garay, J. Anglin, J. Cirac, and P. Zoller, Phys. Rev. Lett. **85**, 4643 (2000).